

Attractor dynamics in networks with learning rules inferred from *in vivo* data - Supplemental Figures

Ulises Pereira and Nicolas Brunel

May 22, 2018

## Supplementary Figures

1	Correlations between input currents corresponding to responses to familiar images . . . . .	3
2	Inferred static transfer functions. . . . .	4
3	Distributions of firing rates for novel stimuli. . . . .	5
4	Inferred dependence on the postsynaptic firing rate of learning rule. . . . .	6
5	Finite size effects . . . . .	7
6	MFT limits and capacity . . . . .	8
7	Maximal capacity in the $(x_f, \beta_f, q_f, A)$ parameter space . . . . .	9

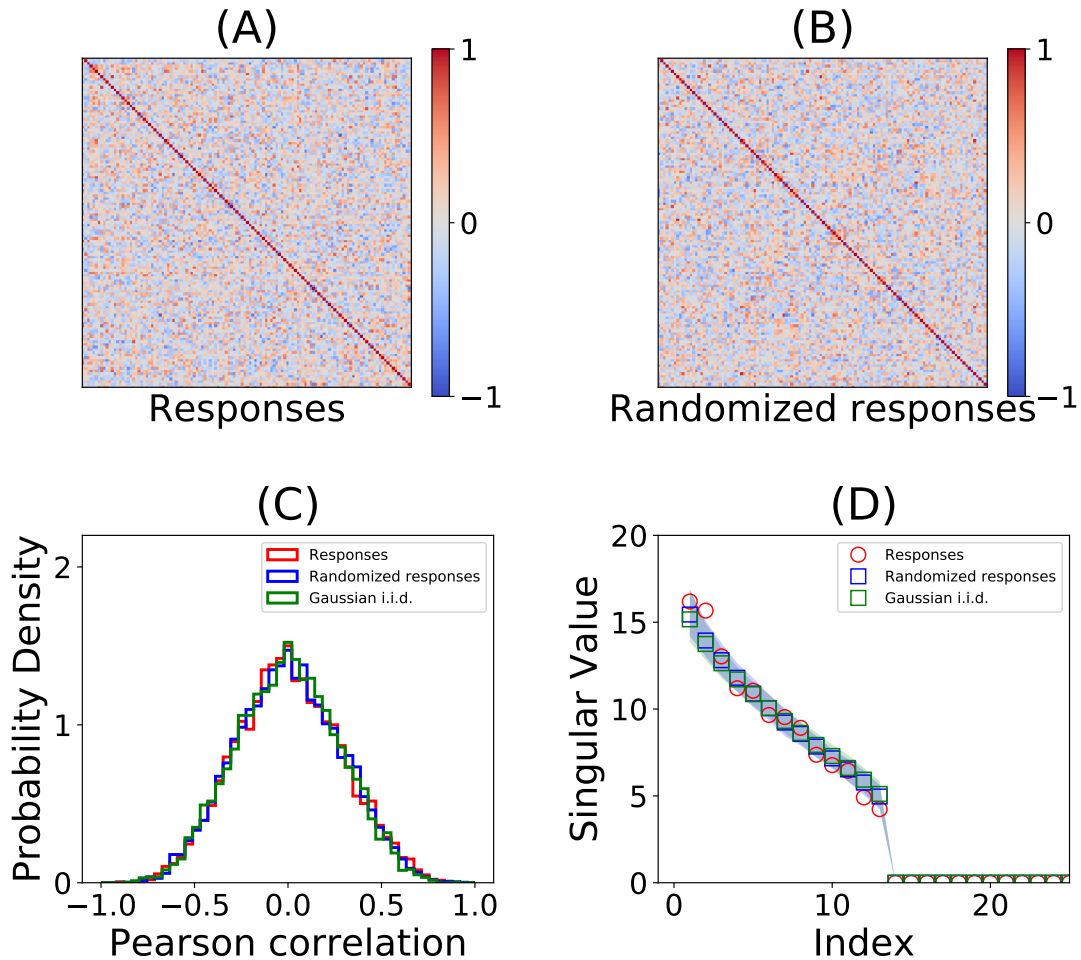


Figure S 1: **Related to Figure 1. Correlations between input currents corresponding to familiar images.** Our theory relies on the assumption that stored patterns are uncorrelated. When correlations between stored patterns are included, the storage capacity of our network drastically decreases. To test this assumption, we computed correlations between input currents corresponding to familiar images. Using the transfer function inferred from novel stimuli (see Fig. S2), we computed for each neuron the input currents that elicit the firing rate responses to each of the 125 familiar images. We then computed the correlations between input currents corresponding to different familiar images. (A) Correlation matrix for the input currents corresponding to the 125 familiar images across the 14 putative excitatory neurons considered in this study. (B) Correlation matrix for the input currents corresponding to the 125 familiar images when the identity of the images are randomly shuffled for each neuron. (C) Histogram of the correlation values for the original correlation matrix in panel A (red), the correlation matrix from the randomized responses in panel B (blue) and from a correlation matrix of input currents drawn independently from a Gaussian distribution with zero mean and unit variance (i.e. Gaussian i.i.d.; green). The diagonal terms were excluded. (D) Largest 20 singular values for correlation matrices in panel A (red), B (green) and from the Gaussian i.i.d. input currents (blue). The opaque blue and green shaded areas correspond to the 95% confidence interval for the singular values across 200 realizations of the correlation matrices of the randomized responses and the Gaussian i.i.d. input currents respectively.

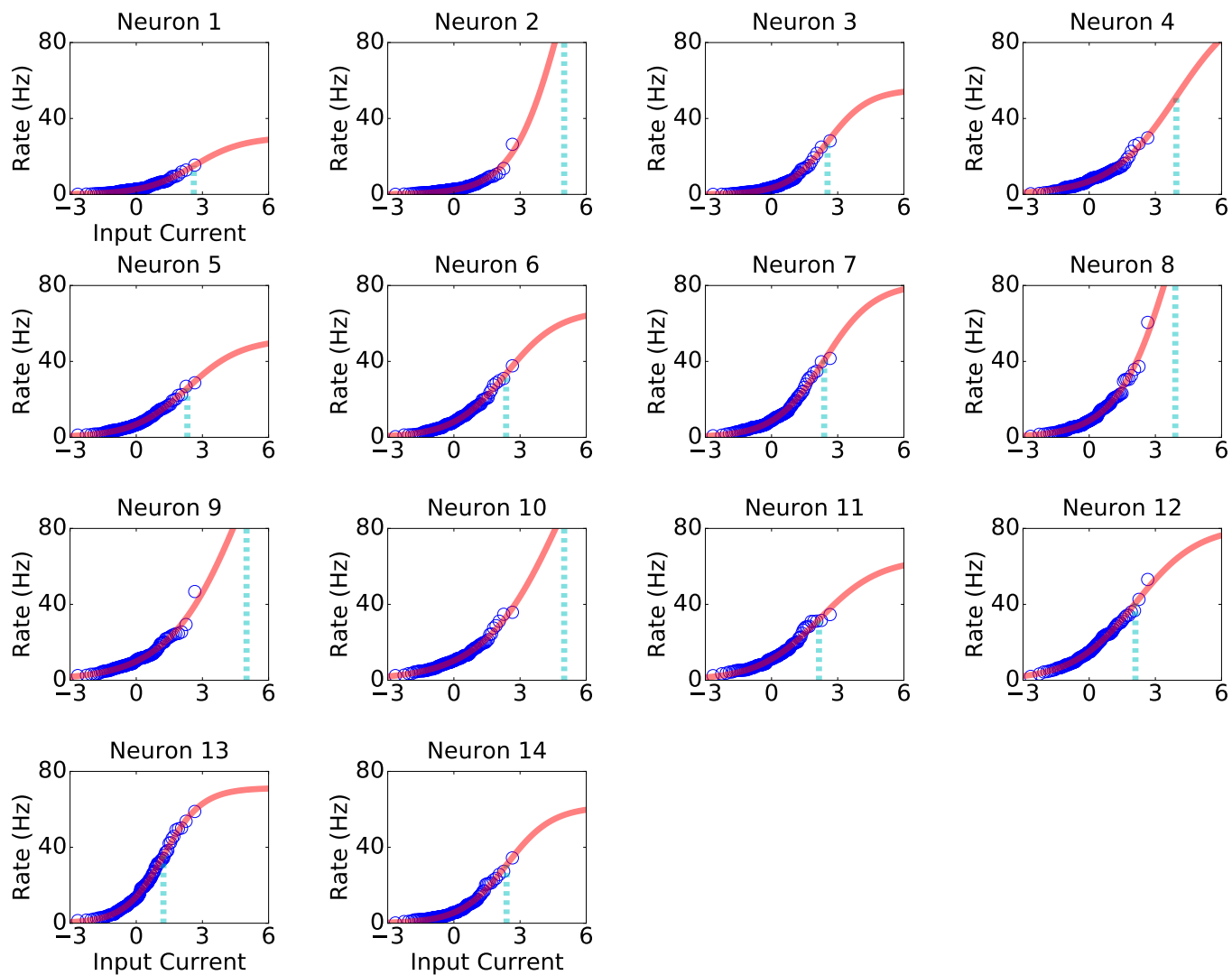


Figure S 2: **Related to Figure 2. Inferred static transfer functions.** The static transfer function  $\phi$  is derived from the distribution of visual responses for novel stimuli for 14 different ITC neurons using the procedure described in Lim et al. (2015). The data (blue circles) was fitted using a sigmoidal function (red line; see Methods, Eq. (3)). Cyan vertical dashed lines indicate the parameter  $h_0$  of the sigmoidal fit. For details, see Methods main text.

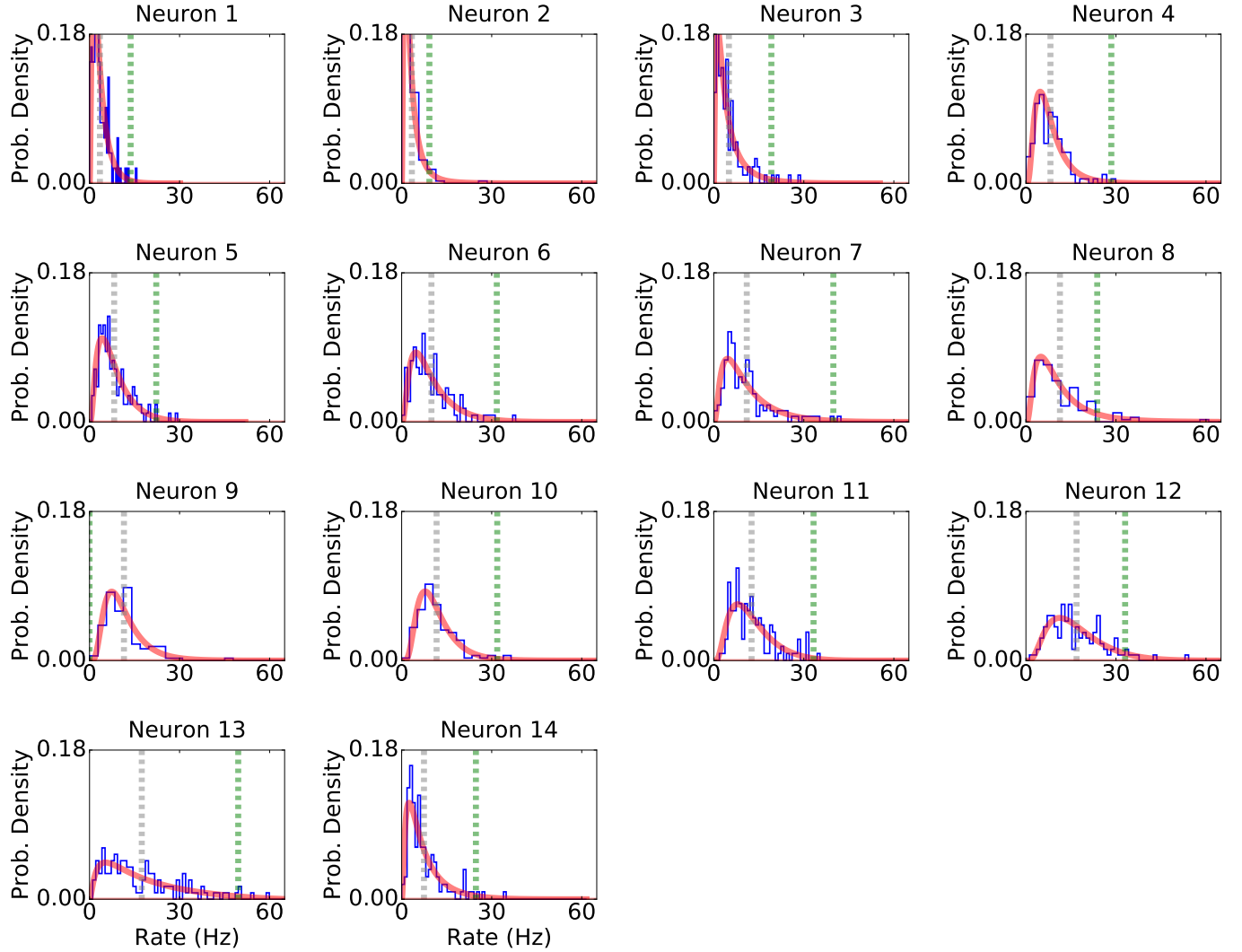


Figure S 3: **Related to Figure 2. Distributions of firing rates for novel stimuli.** Distributions of firing rates in response to 125 novel stimuli for 14 ITC neurons. The firing rate histogram (blue) is plotted together with the distribution of firing rates (red line) obtained when standard normal patterns of current (i.e.  $\xi \sim \mathcal{N}(0,1)$ ) are transformed using the static sigmoidal transfer function fitted in Fig. S2 (i.e.  $\phi(\xi)$ ; see Eq. (3) in Methods). The gray and green vertical dashed lines indicate the mean of the fitted firing rate distribution and the parameter  $x_f$  of the plasticity rule (see Fig. S4).

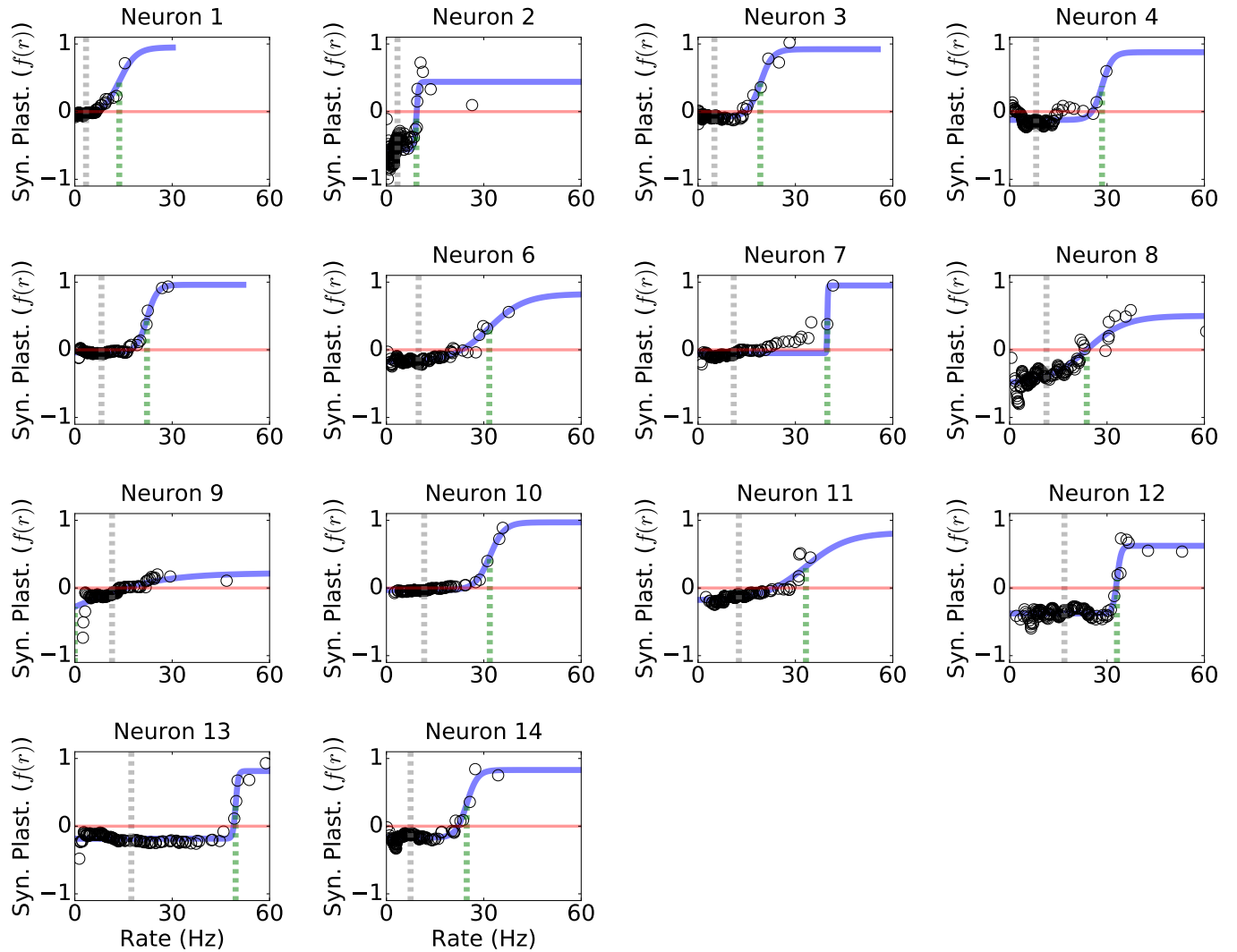


Figure S 4: **Related to Figure 2. Inferred dependence on the postsynaptic firing rate of the learning rule.** The dependence of synaptic plasticity rule on the postsynaptic firing rate (i.e.  $f(r)$ ) is inferred for 14 ITC neurons. The data is indicated with black circles and the sigmoidal fit with a blue line. The red line indicates the threshold between long term potentiation (LTP) and long term depression (LTD). As in Fig. S3, the gray and green vertical dashed lines indicate the mean of the fitted firing rate distribution and the parameter  $x_f$  of the learning rule.

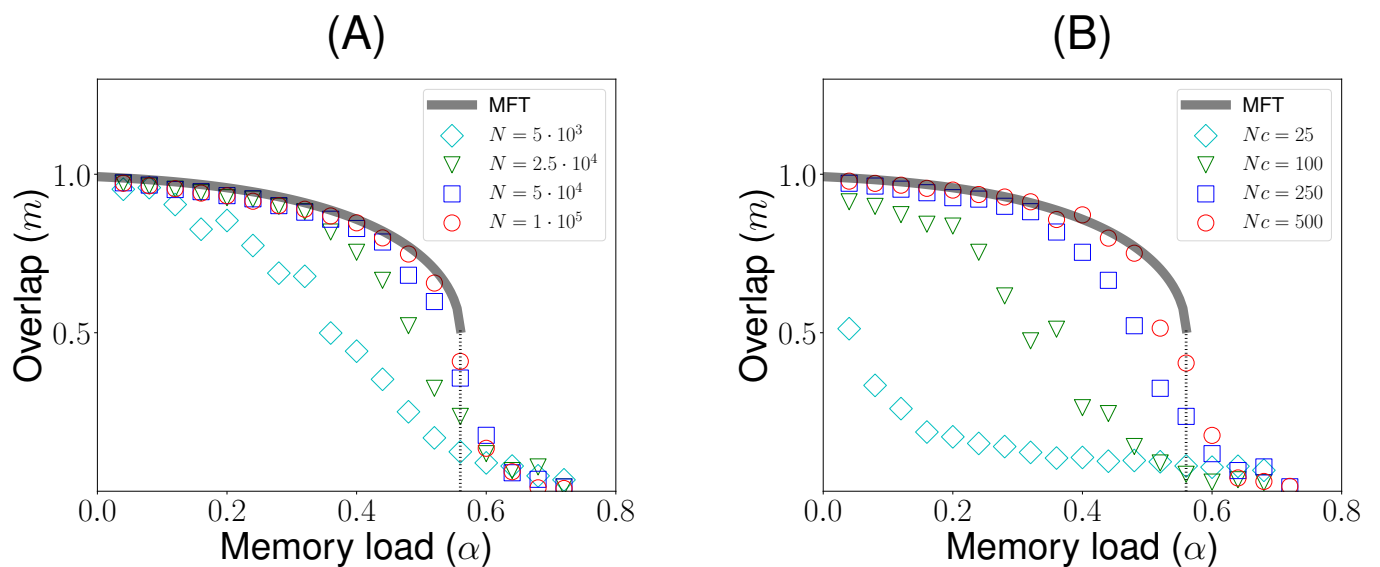


Figure S 5: **Related to Figure 4. Finite size effects.** Our MFT is valid in the large population size ( $N \rightarrow \infty$ ) and large mean in-degree ( $Nc \rightarrow \infty$ ) limit, such that the number of neurons is much larger than the average number of synapses per neuron ( $1 \ll Nc \ll N$ ). Here we explore the effects of varying the population size ( $N$ ) and mean in-degree ( $Nc$ ) on the overlap in retrieval states. **(A)** Overlap as a function of memory load  $\alpha$  for various values of  $N$ , at fixed  $cN = 250$ . Grey curve: MFT. Symbols: average overlap (computed from 50 realizations) in simulations with population sizes  $N = 5000, 25000, 50000, 100000$ . **(B)** Overlap as a function of memory load  $\alpha$  for various mean in-degrees, for  $N = 25000$ . Grey curve: MFT. Symbols: average overlap in simulations with average mean in-degrees  $Nc = 25, 100, 250, 500$ . Parameters for  $\phi$ ,  $f$  and  $g$  are chosen as in Fig. 4A on the main text.

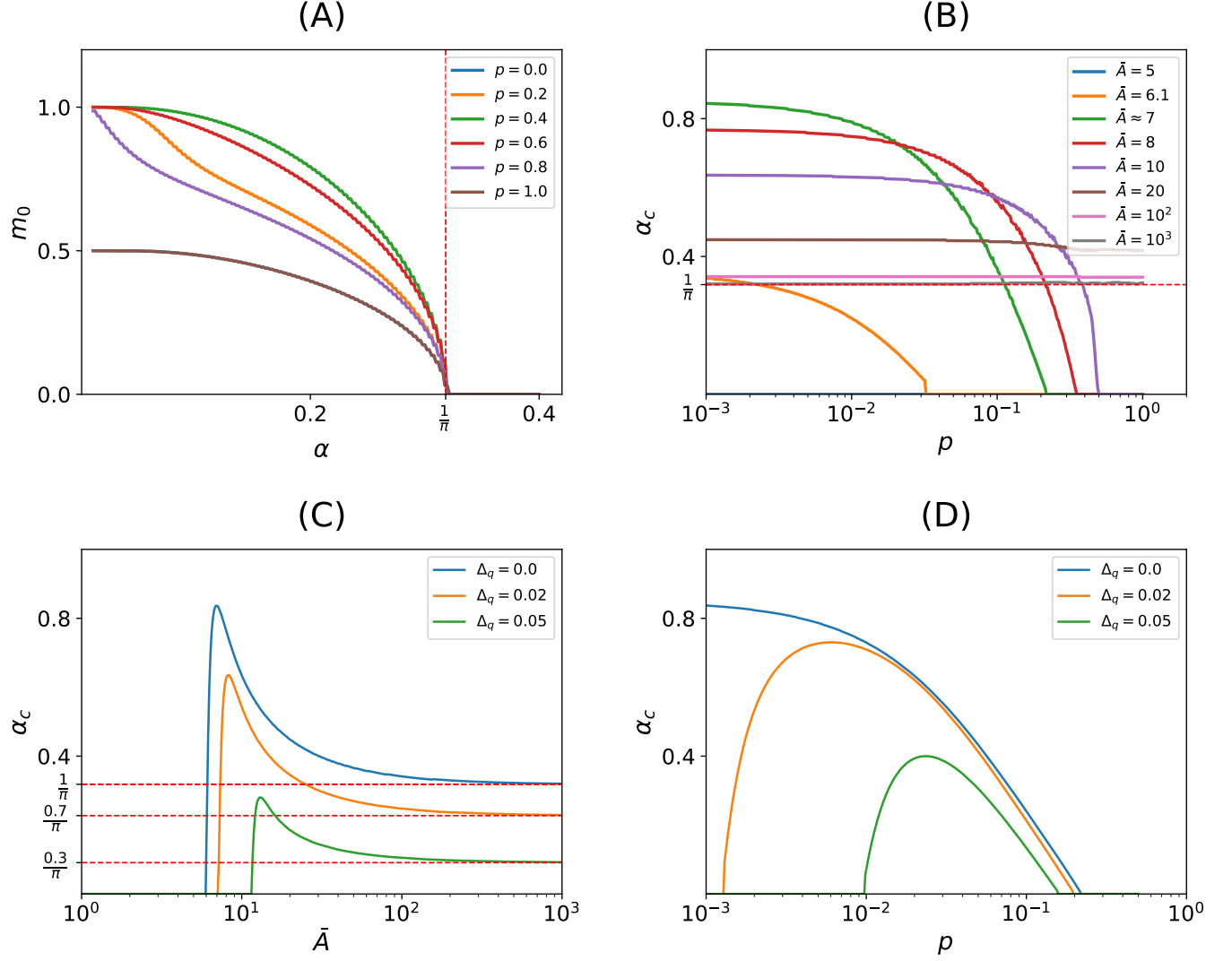


Figure S 6: **Related to Figure 5. MFT limits and capacity.** (A) Overlap vs load  $\alpha$  in the limit  $q_g \rightarrow q_f$  and  $\bar{A} \rightarrow \infty$  (see (37) and (38) on section 3.2 of Methods S1) for  $p = 0, 0.2, 0.4, 0.6, 0.8, 1$  ( $p = 1 - q_g$ ). In this limit, the mean field equations (see Eq. (20) and (21) in Tsodyks (1988)) with  $\theta_0 = 0$  are recovered. (i.e.  $\alpha_c \approx \frac{\theta_0^2}{2p \log(1/p)}$ ) is not attainable since  $\theta_0 = 0$ . The capacity is  $\alpha_c = 1/\pi$  for all  $p$ . (B) Capacity vs  $p$  for  $\bar{A} = 5, 6.1, 6.95, 8, 10, 20, 100, 1000$  (see Eq. (35) and (36) on section 3.2 of Methods S1). For a fixed  $\bar{A} \sim \mathcal{O}(1)$ , capacity is maximized in the sparse coding limit (i.e.  $p \rightarrow 0$ ).  $\bar{A} \approx 6.95$  and  $p \rightarrow 0$  leads to the maximal capacity in the  $\bar{A}$ - $p$  plane, with  $\alpha_c \approx 0.85$  (see green curve). For  $\bar{A} \rightarrow \infty$ , which implies  $\frac{r_m}{p(1-p)} \ll A$ , the capacity is  $\alpha_c = 1/\pi$  for all  $p$  (see gray curve and dashed red line) as shown in panel A. (C) Capacity vs  $\bar{A}$  for  $p = 10^{-3}$  and  $\Delta_q = q_g - q_f = 0, 0.02, 0.05$  (see Eq. (33) and (34) on section 3 of Methods S1). For  $\Delta_q = 0$  the mean field equations are the same as in panel B with  $p = 10^{-3}$ , showing the maximal capacity  $\alpha_c \approx 0.85$  at  $\bar{A} \approx 6.95$ . Increasing  $\Delta_q$ , which implies  $q_f < q_g$ , produces a rapid decrease in the capacity (see orange and green curves). For  $\bar{A} \rightarrow \infty$  the capacity decreases rapidly as  $\alpha_c = \eta^2/\pi$  (see dashed red lines) as shown in section 3.1 of Methods S1 (see Eq. (40)). (D) Capacity vs  $p$  for  $\bar{A} = 6.95$  and  $\Delta_q = 0, 0.02, 0.05$  (see Eq. (33) and (34) on section 3 of Methods S1). As in panel C, the capacity decreases rapidly as  $\Delta_q$  increases. For  $0 < \Delta_q$  the maximal capacity occurs at non-zero  $p$  (the capacity curve becomes concave). This is similar to what is observed for sigmoidal  $f$  and  $g$  (see Fig. 5 main text), where the maximal capacity is obtained for a finite threshold and a non-zero value of  $p$ .



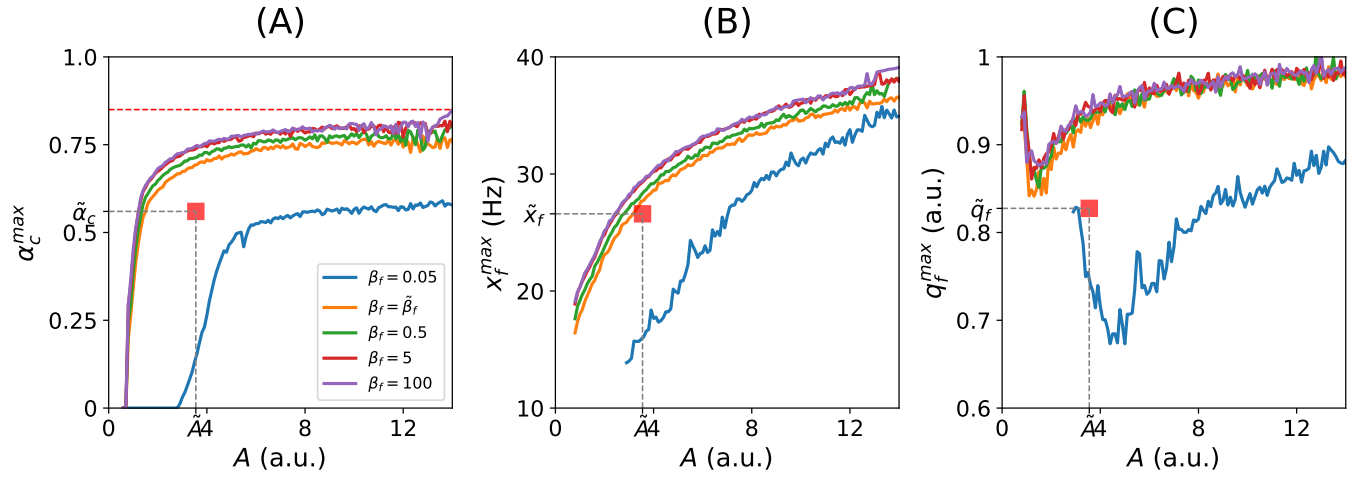


Figure S 7: **Related to Figure 5. Maximal capacity in the  $(x_f, \beta_f, q_f, A)$  parameter space.** Numerical search of the maximal capacity using the Nelder-Mead algorithm for sigmoidal  $f$  and  $g$  (see Eq. (8) and (10) on the main text) with  $x_g = x_f$  and  $\beta_g = \beta_f$ . For four representative values of the slope  $\beta_f$  ( $\beta_f = \{0.05, \tilde{\beta}_f, 0.5, 5\}$  where  $\tilde{\beta}_f$  is the median of the best-fit slopes), the maximal capacity was searched in the  $(x_f, q_f)$  parameter space for fixed values of  $A$  in a grid. Starting with the largest value of  $A$  in the grid, we used the previous maximal capacity point  $(x_f^{max}, q_f^{max})$  as the initial condition for searching the maximal capacity of the next value of  $A$ . In this way, we smoothly followed the maximal capacity in the  $(x_f, q_f, A)$  parameter space. The maximal capacity increases monotonically with  $\beta_f$ . **(A)** Maximal capacity ( $\alpha_c$ ) vs  $A$  for different values of  $\beta_f$ . The maximal capacity approaches asymptotically the value found in Fig. S6.B (i.e.  $\alpha_c \approx 0.85$ , see dashed red line). The capacity for the median best-fit parameters (see red square) is smaller but comparable with the maximal capacity in the  $(x_f, \beta_f, q_f, A)$  parameter space. **(B)** Optimal threshold ( $x_f$ ) vs  $A$ . Red square: Median best-fit threshold. **(C)** Optimal saturation ( $q_f$ ) vs  $A$ . Red square: Median best-fit saturation.